Supporting Information

Somatosensitive Film Soft Crawling Robots Driven by Artificial Muscle for Load Carrying and Multi-Terrain Locomotion

*Zhongsheng Liu,[1] Rui Zhang,[2] Yicheng Xiao,[1] Jiatian Li,[1] Wang Chang,[1] Dong Qian,[2] Zunfeng Liu[1]**

[1]*State Key Laboratory of Medicinal Chemical Biology, College of Pharmacy, Key Laboratory of Functional Polymer Materials, Nankai University, Tianjin 300071, China*

[2]*Department of Mechanical Engineering University of Texas at Dallas Richardson, TX 75080, USA*

**Corresponding author E-mail: liuzunfeng@nankai.edu.cn*

The supporting information includes:

1. Simulation of Artificial Muscles by Finite Elemental Analysis

1.1.Thermomechanical modeling of the artificial muscles

Three-dimensional transient heat transfer models are established for the artificial muscles using the commercial finite element analysis software ABAQUS (version 6.14). Temperature change in the muscles is contributed by both the electrothermally generated heat flux and the natural convection of the ambient air at room temperature. Both the NCY muscle and the SCN muscle are investigated here. For the NCY muscle, only a small fraction of the exterior surface of the nylon 6 fiber is in contact with the CNT yarn (Fig. $2d_2$). For the SCN muscle, the entire exterior surface of the fiber is coated with a thin layer of SWNT (Fig. $2d_4$). In the simulations, the applied surface heat fluxes are consistent with the experiments. For the convective boundary condition, a convective heat transfer coefficient of 50 W/(m^2 K) is employed. Material parameters for nylon 6 fiber are given as follows: the volumetric mass density is 1.13 g/cm^3, the thermal conductivity is 0.28 W/(m K), and the specific heat is 1700 J/(K kg). To improve the computational efficiency, we model only a small segment of the muscles with around 1,500 DC3D8 elements, and the adiabatic boundary condition is applied to the cross-sections. Figure $2d_3$ shows that temperature distribution in the NCY muscle is non-uniform, while the temperature distribution in the SCN muscle is quasi-uniform (Fig. $2d_5$). Volume averaged temperature responses are shown in Fig. S4 for the NCY muscle at different loads and input power, which demonstrate good agreement with experimental measurements. Similarly, Fig. S5 shows the average temperature responses in the SCN muscle, which also match well with the experimental results.

For mechanical actuation, we employ a closed-form model developed by Haines *et*

al.[1] In this model, the fiber length *l*, fiber diameter *d*, and the helically oriented polymer chain length λ are related through

$$\lambda^2 = \left[\left(\pi d T \right)^2 + 1 \right] l^2 \quad \text{* MERGEFORMAT (1)}$$

where *T* is the twist density.

Upon heating, polymer chains in nylon 6 will expand in radial direction and contract in axial direction, which can be accommodated by changes in length, diameter, and twist. The change in length is considered small and the following equation for untwisting is obtained

$$\Delta T = \left(\frac{\Delta \lambda}{\lambda} \frac{1}{\cos^2 \alpha_f} - \frac{\Delta d}{d} \right) T \quad \text{* MERGEFORMAT (2)}$$

where the bias angle $\alpha_f = \tan^{-1}\left(\pi d T \right)$.

The equation * MERGEFORMAT (2) can be further simplified as

$$\Delta T = \left(\alpha_\lambda \frac{1}{\cos^2 \alpha_f} - \alpha_d \right) \Delta \theta \cdot T \quad \text{* MERGEFORMAT (3)}$$

where α_λ and α_d are the coefficients of thermal expansion of the polymer chains in axial and radial directions, respectively. $\Delta \theta$ is the volume-averaged temperature change obtained from the previous transient heat conduction simulation. Note that the coefficients of thermal expansion are approximated in this study. For the NCY muscle, we employ $\alpha_\lambda = -240 \times 10^{-6}\ \mathrm{K}^{-1}$ and $\alpha_d = 240 \times 10^{-6}\ \mathrm{K}^{-1}$. For the SCN muscle, we employ $\alpha_\lambda = -300 \times 10^{-6}\ \mathrm{K}^{-1}$ and $\alpha_d = 350 \times 10^{-6}\ \mathrm{K}^{-1}$.

The contraction actuation mechanism of twisted, mandrel-coiled polymer fiber is explained in the literature.[1] The contraction stoke is quantified by

$$\Delta L = \frac{l^2}{N} \Delta T \quad \text{* MERGEFORMAT (4)}$$

where *l* is the twisted fiber length, *N* is the number of coil turns.

Predictions on contraction actuation using the above equations are presented in Figs. S4 and S5 for the NCY muscle and the SCN muscle, respectively. An overall good agreement with the experiment is observed.

Finally, Hooke's law is employed to compute the contraction force:

$$F = k(\theta)\Delta L, \qquad \text{* MERGEFORMAT (5)}$$

where $k(\theta)$ is the temperature-dependent stiffness of the muscles. Numerical experiments show that it is critical to consider a temperature-dependent stiffness since the nylon 6 fiber becomes softer upon heating (Fig. 2b) and a constant stiffness at room temperature will lead to an over-estimation of the contraction force. The temperature-dependent stiffness is derived by numerically fitting the experimentally measured load-displacement curves of the artificial muscles at different temperatures (Fig. 2b). The predicated contraction forces using the established semi-analytical model are shown in Fig. 2e and demonstrate good match with the experiment.

2. Supplementary figures

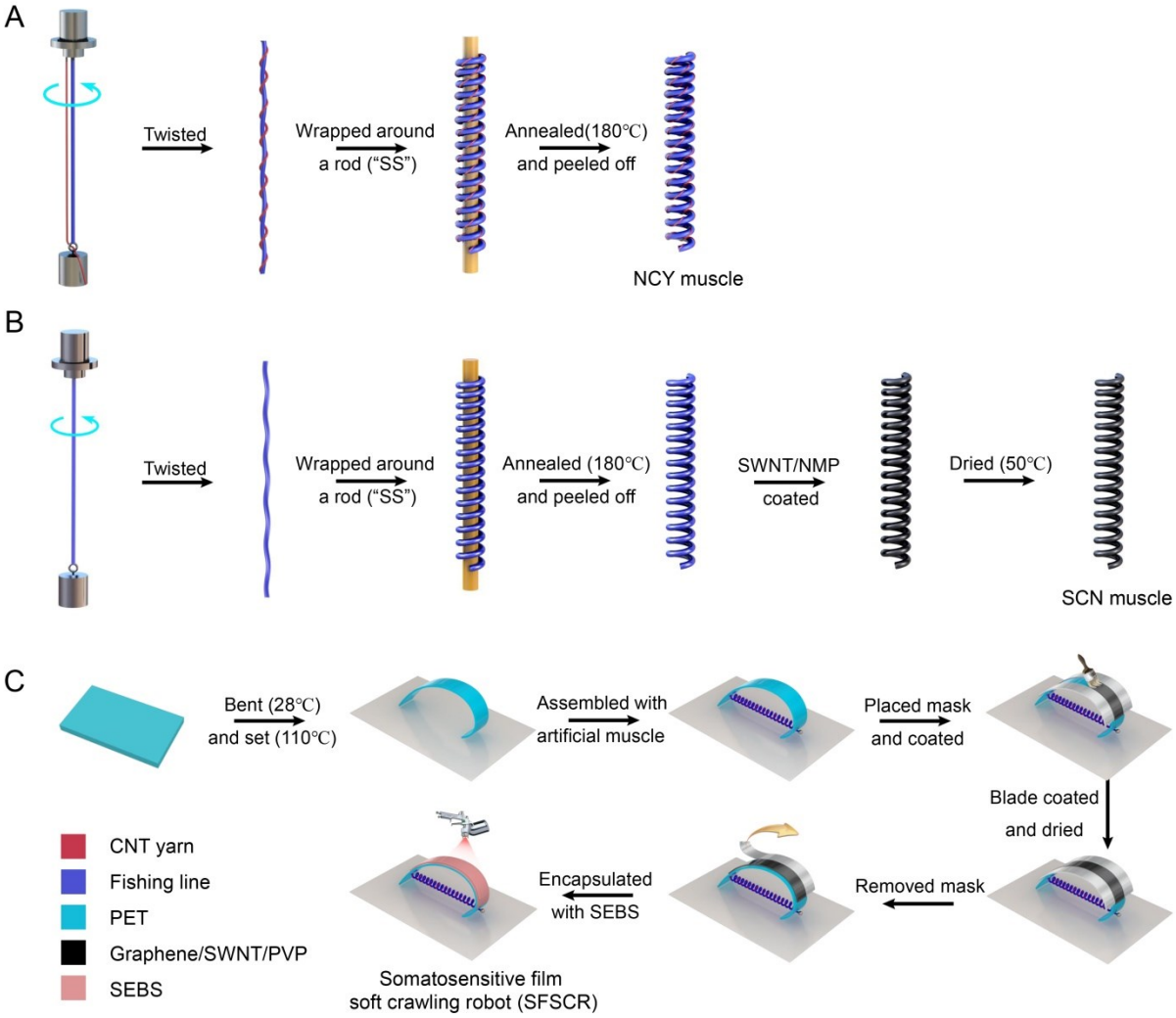

Figure S1. The fabrication of muscles and the SFSCR. Schematic illustration showing the fabrication process of the NCY muscle (A), the SCN muscle (B), and the SFSCR (C).

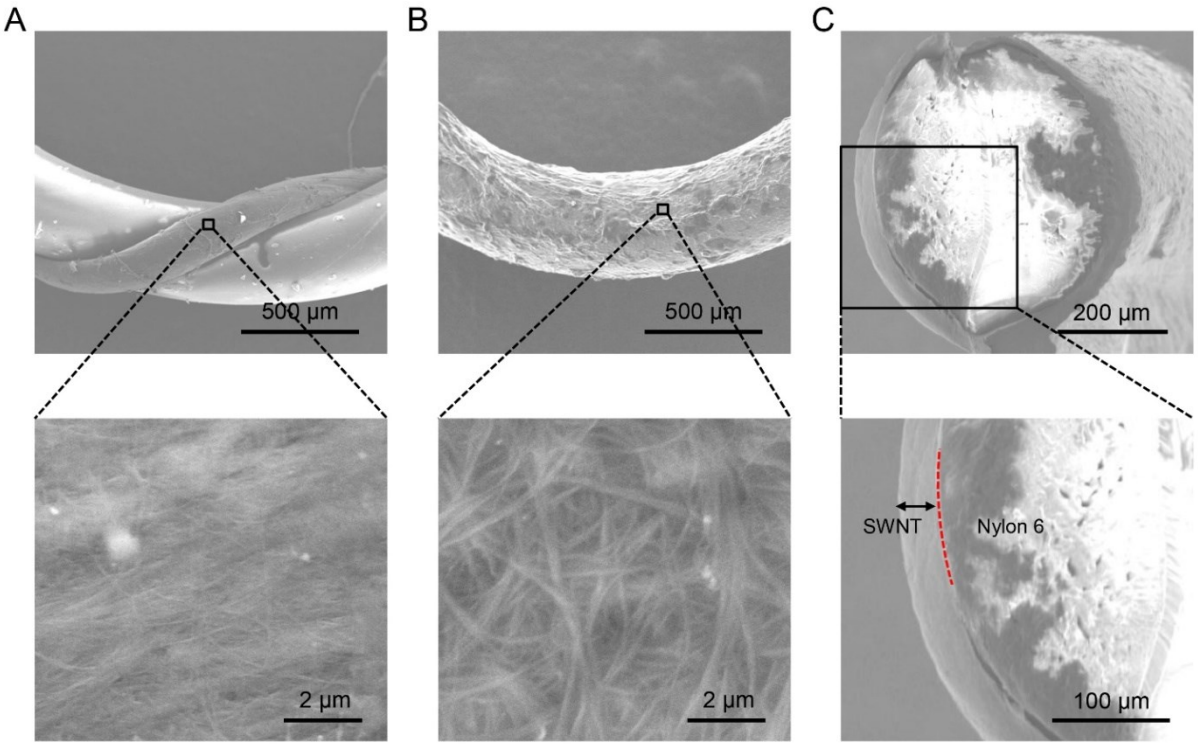

Figure S2. SEM images of artificial muscles. (A) SEM images showing the top view of the surface of the NCY muscle and magnification of the CNT yarn. (B, C) SEM images showing low and high magnification of the top view (B) and cross-section (C) of the SCN muscle.

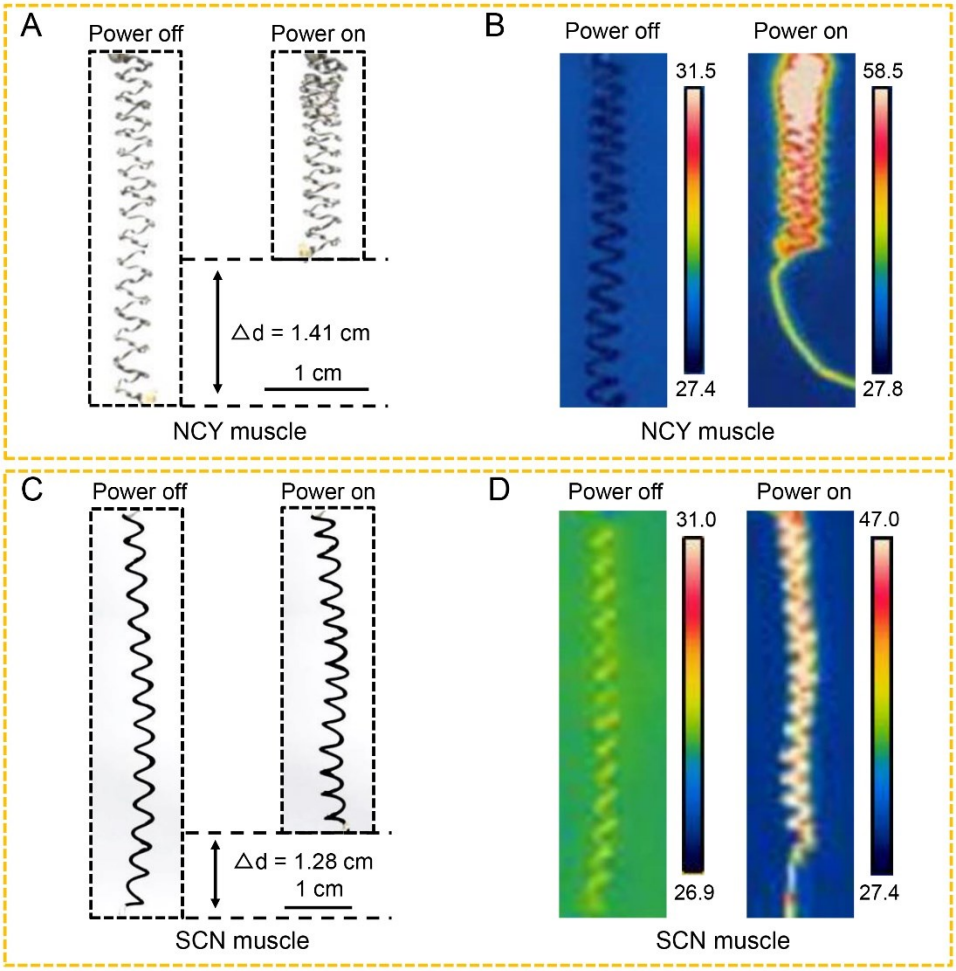

Figure S3. Actuation processes of artificial muscles. (A, C) Optical and (B, D) infrared images of the NCY muscle (A, B) and the SCN muscle (C, D) before and after the electric power is on.

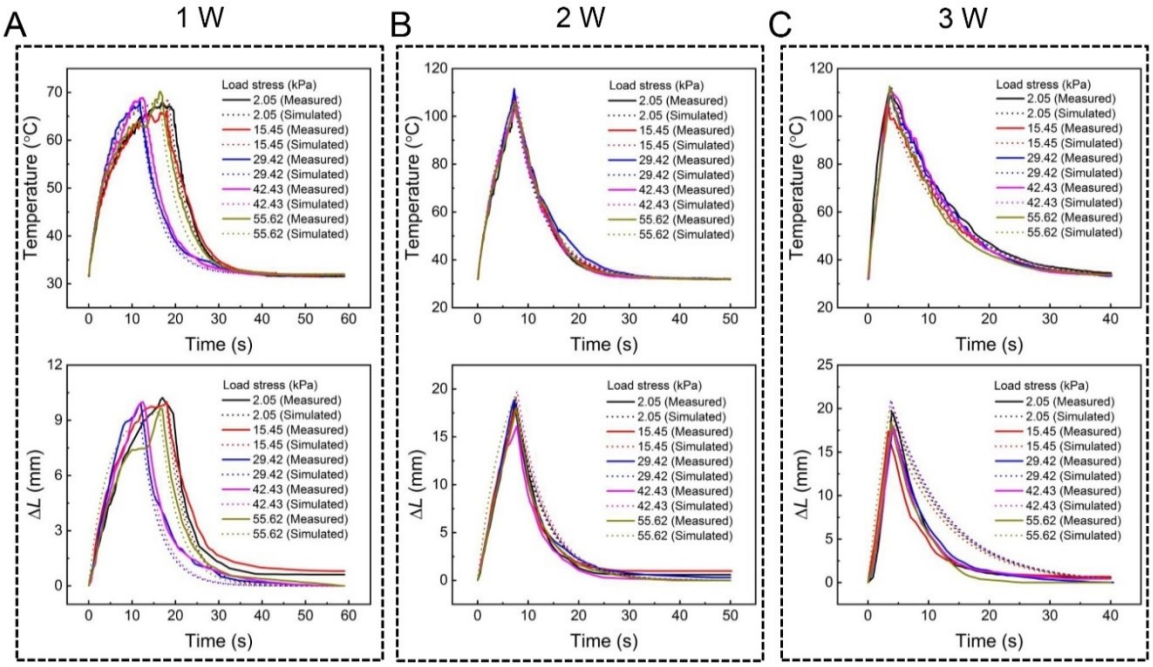

Figure S4. Actuation performances of the NCY muscle. Experimental and simulation results of the temperature (top) and length contraction (ΔL, bottom) as a function of time for the NCY muscle at different loads by applying 1 W (A), 2 W (B), and 3 W (C) electric power. The electric power was switched off as the muscle contracted to a certain length to avoid coil contact.

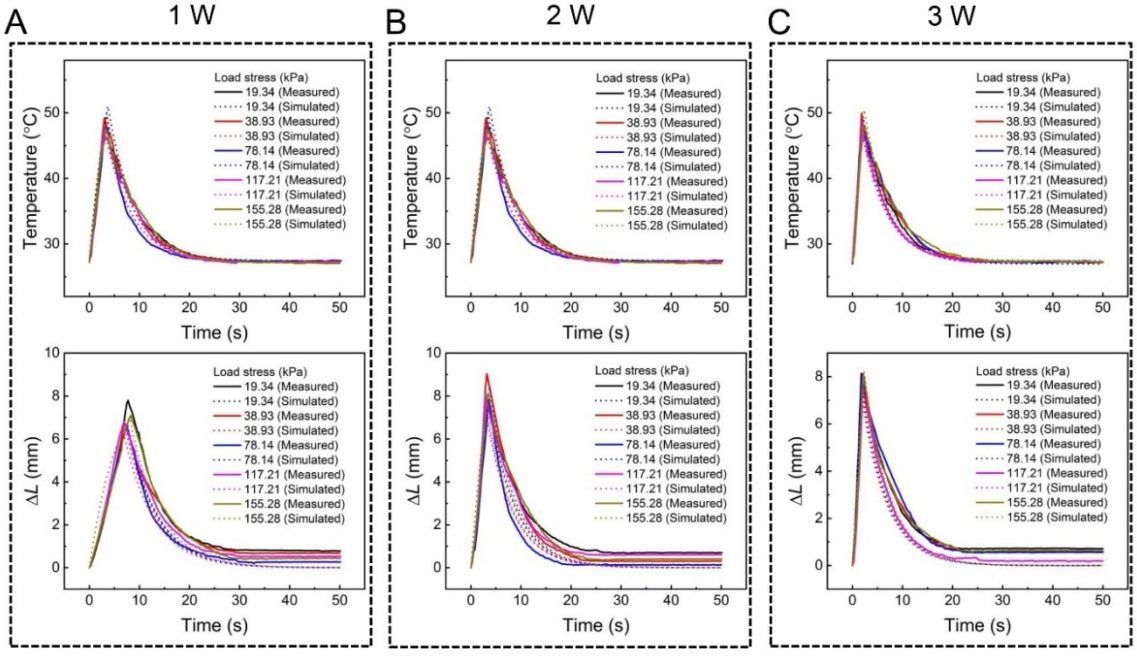

Figure S5. Actuation performances of the SCN muscle. Experimental and simulation results of the temperature (top) and length contraction (ΔL, bottom) as a function of time for the SCN muscle at different loads by applying 1 W (A), 2 W (B), and 3 W (C) electric power. The electric power was switched off as the muscle contracted to a certain length to avoid coil contacting.

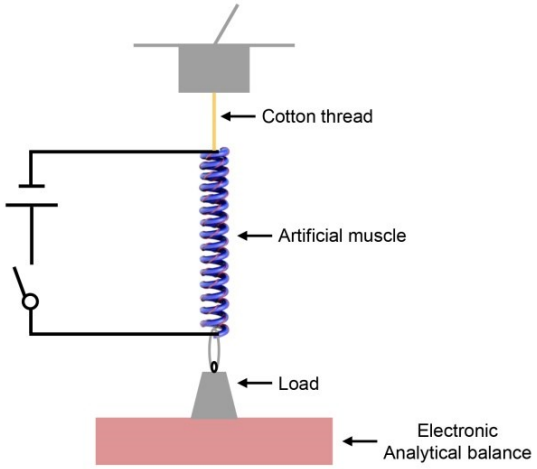

Figure S6. Schematic illustration of the setup for measuring the contraction force of the artificial muscle.

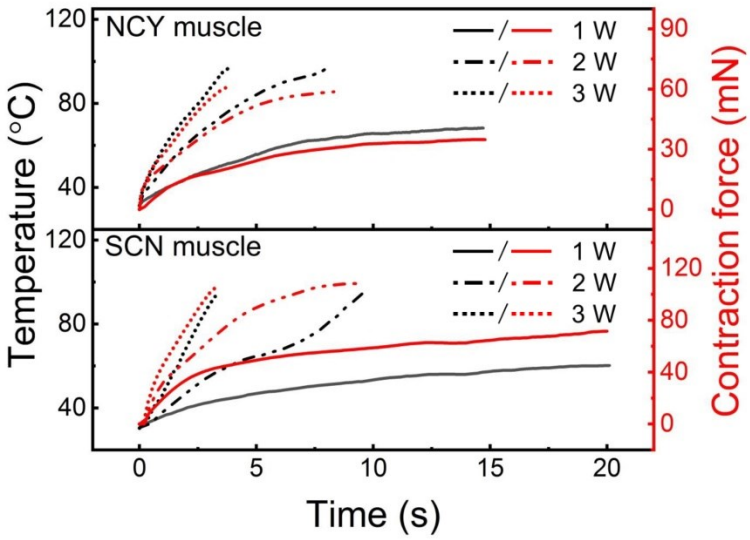

Figure S7. Time dependence of surface temperature and contraction force for the NCY muscle and the SCN muscle at different power measured using the setup shown in Fig. S6.

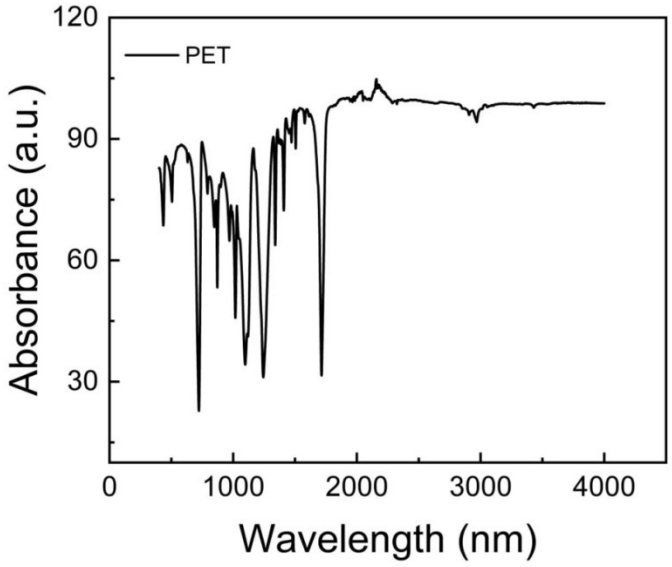

Figure S8. Fourier transformed infrared spectroscopy of the PET film.

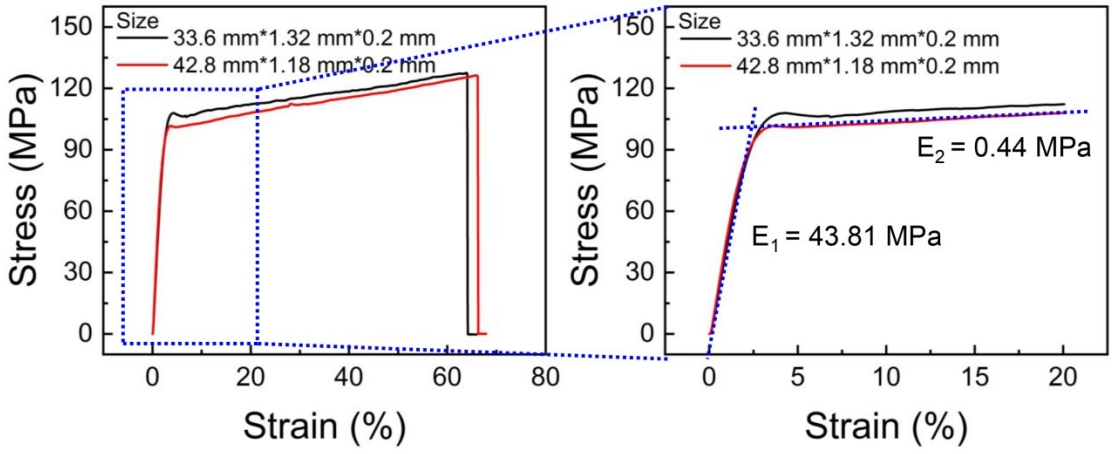

Figure S9. Stress-strain curves of the PET film.

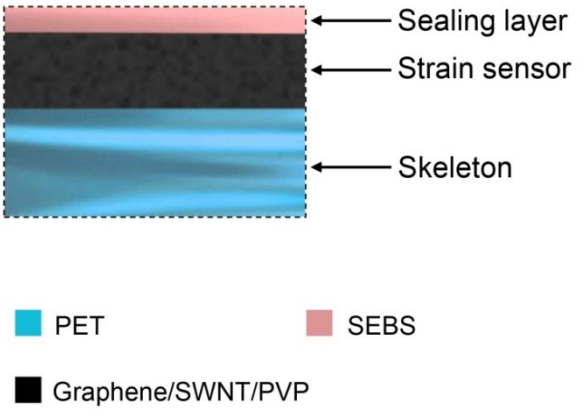

Figure S10. Schematic cross-sectional image of the SFSCR. Schematic illustration of the cross-sectional view of the structure of the SFSCR containing PET film serving as the skeleton, graphene/SWNT/PVP composite serving as the strain sensor, and SEBS serving as the sealing layer of the strain sensor.

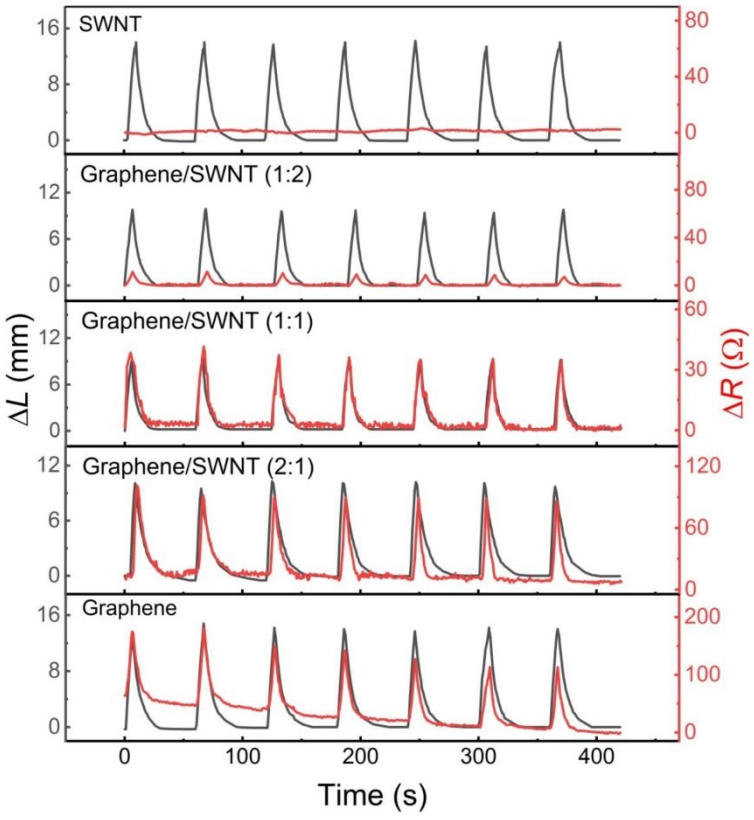

Figure S11. Sensing performances of strain sensors with different compositions. The resistance change (ΔR) of the strain sensor during distance change (ΔL) between the two legs of the SFSCR as a function of time for different compositions of the strain sensor.

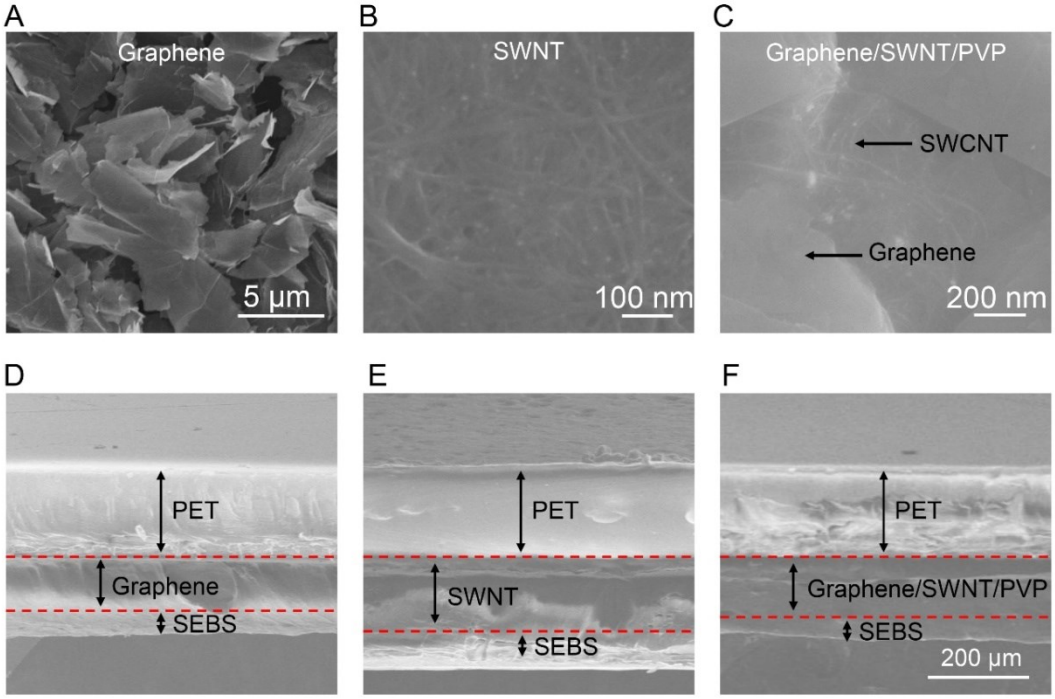

Figure S12. SEM images of strain sensors. (A-C) SEM images showing the surface of the graphene/SWNT/PVP composite film with mass ratio of graphene/SWNT of 1: 0 (A), 0: 1 (B), and 2: 1 (C). (D-F) SEM images showing the cross-section of the graphene/SWNT/PVP composite layer coated on PET thin film and encapsulated with the SEBS layer, with mass ratio of graphene/SWNT of 1: 0 (D), 0: 1 (E), and 2: 1 (F).

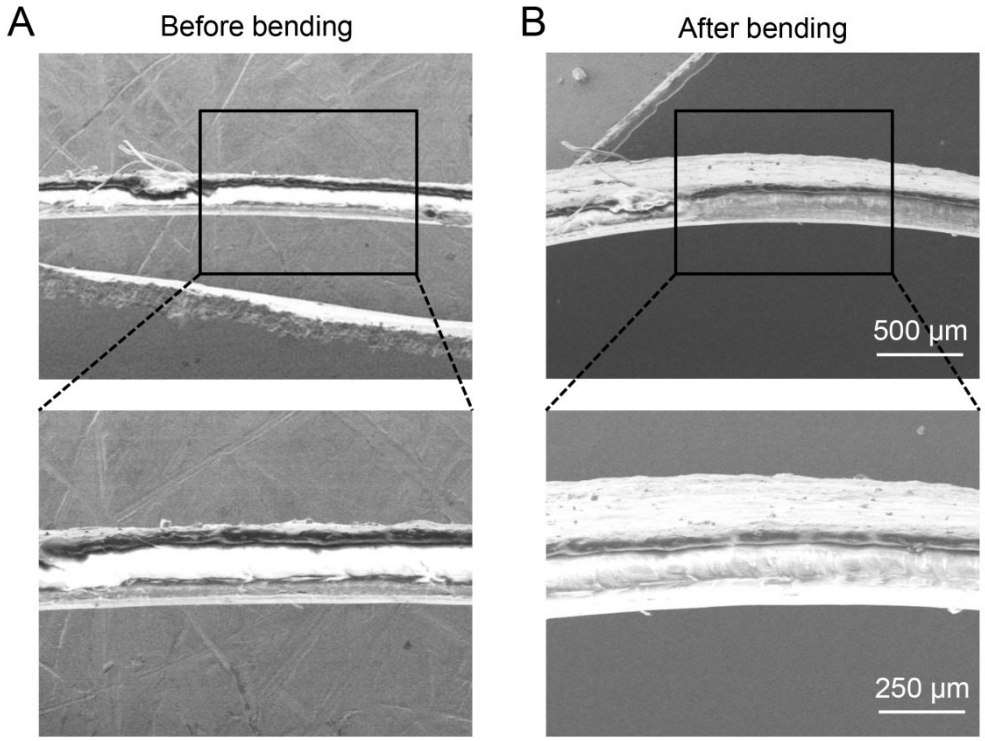

Figure S13. The cross-sectional SEM images of the strain sensor on the skeleton before (A) and after (B) bending. The sensor was encapsulated in a SEBS thin layer.

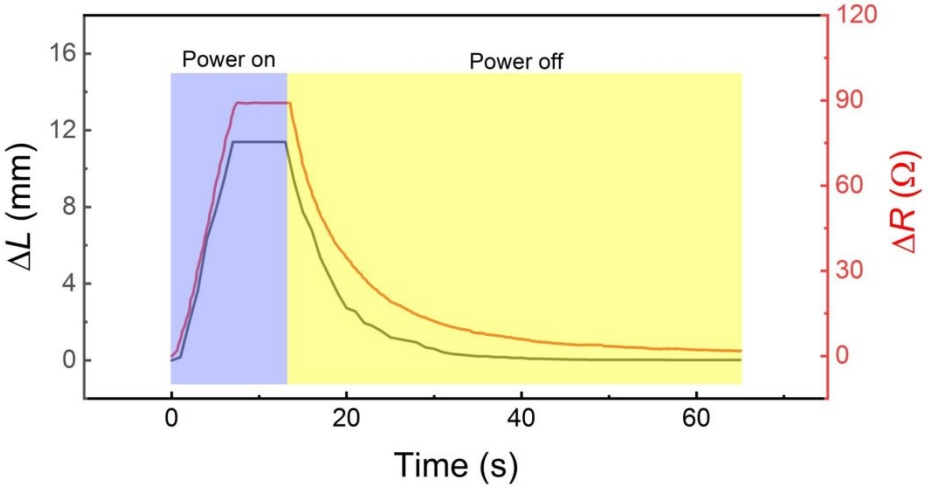

Figure S14. Sensing performances of the strain sensor on the SFSCR. The resistance change (ΔR) of the strain sensor (with a mass ratio of graphene/SWNT of 2: 1) and the distance change (ΔL) between the two legs of the SFSCR during electrothermal actuation by applying 2 W electric power on the NCY muscle followed by removing the electric power. The flat region of the curves indicated that the length was manually kept constant as the length contracted to a certain length to avoid coil shortage induced by coil contacting.

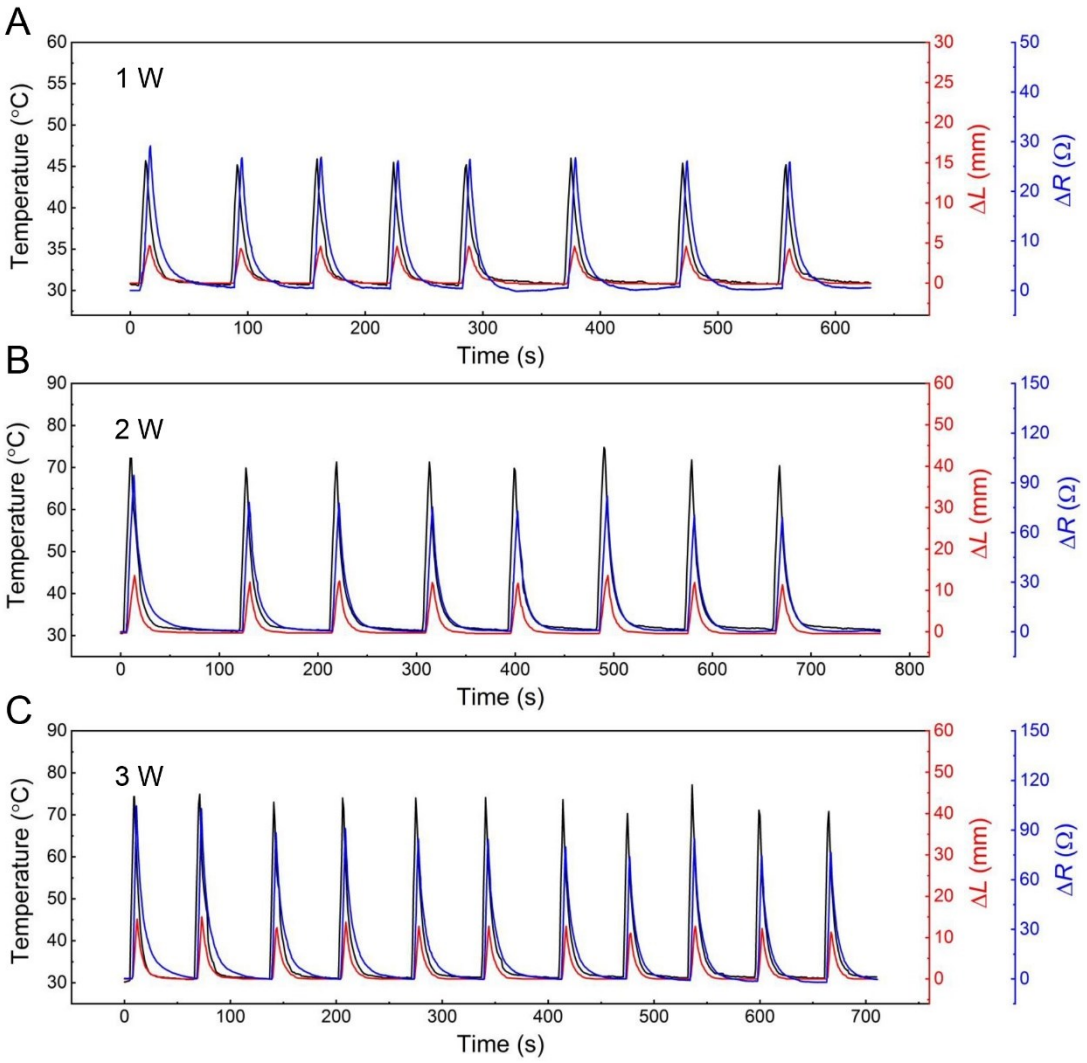

Figure S15. Cyclic Testing of the SFSCR (NCY muscle). The resistance change (ΔR) of the strain sensor, displacement between the two legs of the SFSCR, and muscle temperature as a function of time during cyclic bending and unbending of the SFSCR by applying electric power of 1 W (A), 2 W (B), and 3 W (C) on the NCY muscle.

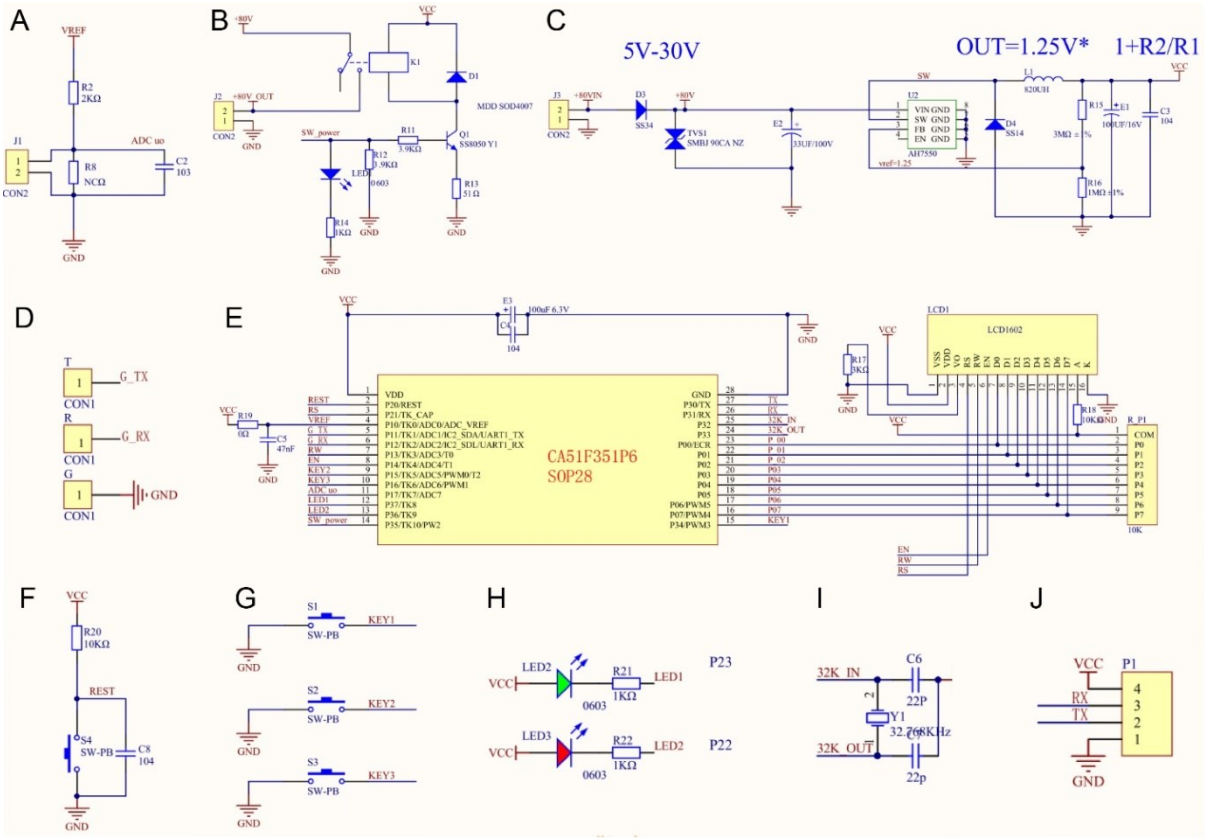

Figure S16. Circuit diagrams of the controller. Circuit diagrams of the controller for (A) resistance measurement, (B) relay, (C) power supply, (D) lead-out pad, (E) main control, (F) reset, (G) button setting, (H) LCD indicator, (I) crystal oscillator, and (J) serial circuit.

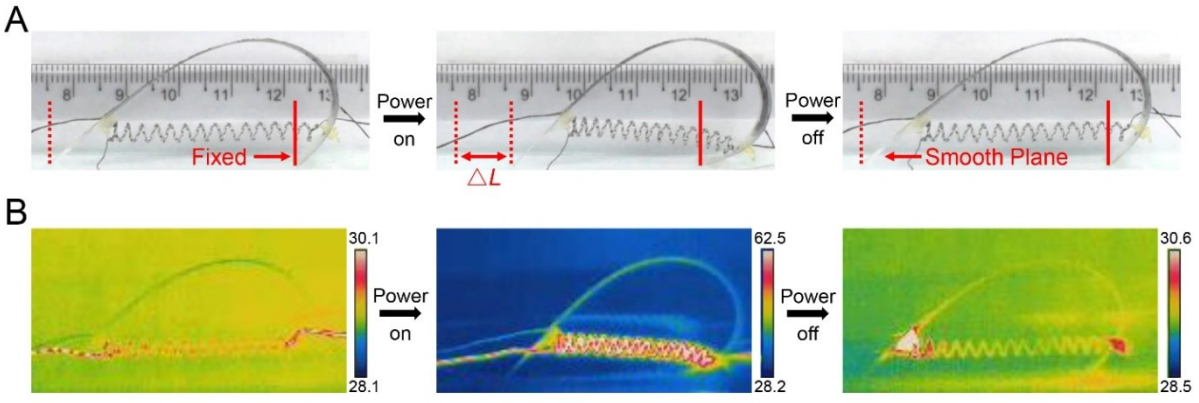

Figure S17. Actuation of the SFSCR by electro-heating during one cycle. (A) Optical and (B) infrared images showing self-crawling of the SFSCR (NCY muscle) with the foreleg attached on the surface and not allowed to move during one cycle of actuation by applying 2 W electric power.

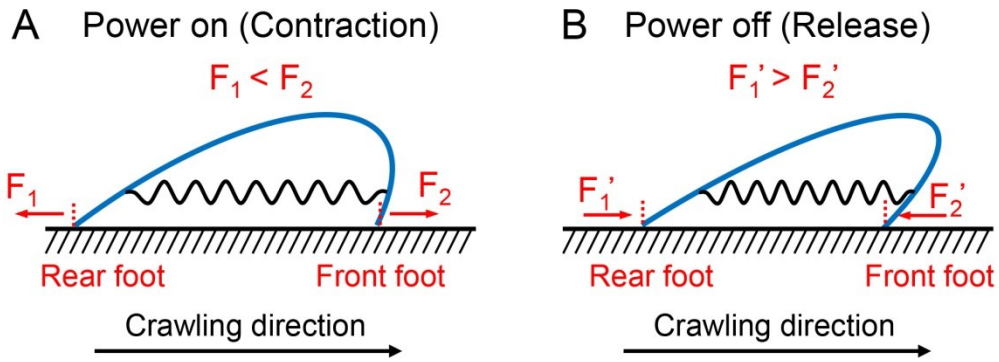

Figure S18. Force analysis diagrams of the SFSCR during power on (A) and power off (B).

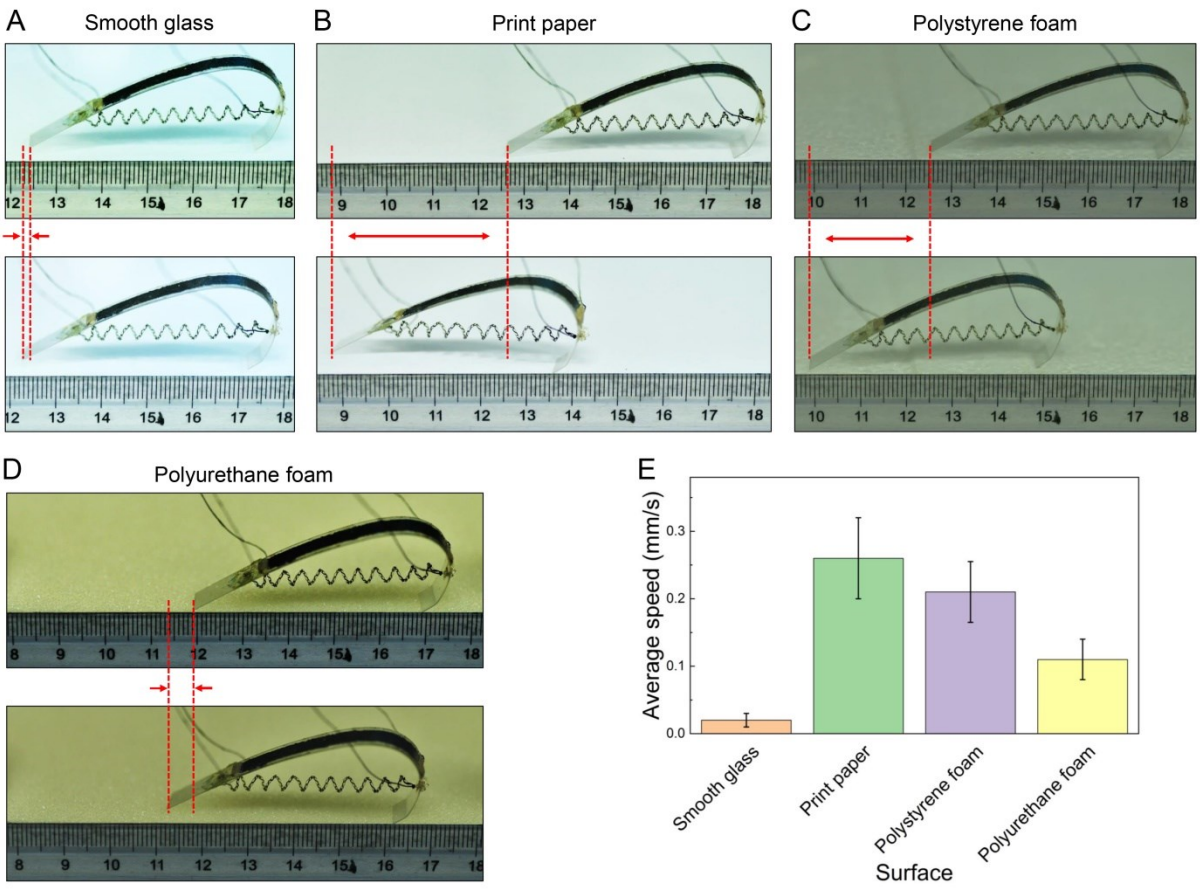

Figure S19. Locomotion of the SFSCR on surfaces with different roughness. (A-D)The surfaces including smooth glass (A), print paper (B), polystyrene foam (C), and polyurethane foam (D). (E) Average crawling speed on these surfaces.

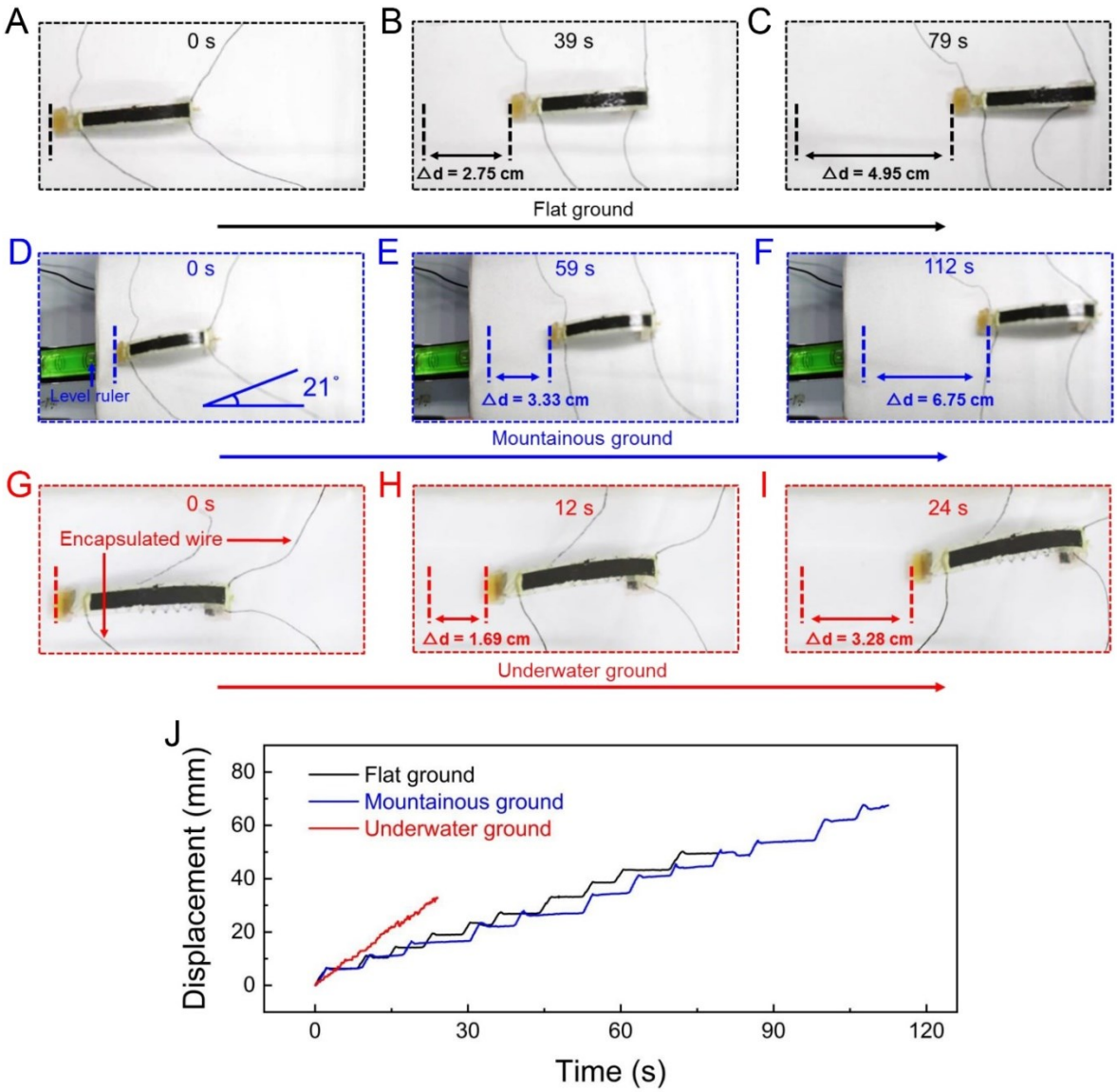

Figure S20. Crawling properties of the SFSCR in different terrains. (A-I) Photographs during self-crawling of the SFSCR (NCY muscle) on flat (A-C), mountainous (D-F), and underwater surfaces (G-I) without using a zigzag surface pattern. (J) Displacement of the SFSCR as a function of time during self-crawling in different terrains without using zigzag surface pattern.

3. Supplementary Table

Table S1. Summary of the typical film soft crawling robot from reported literatures.

Materials	Year	Crawling speed ($mm \cdot s^{-1}$)	Biomimetic design (Muscle +skeleton + sensor with feedback control; Yes or No)	Somatos-ensition (Yes or No)	Load-carrying capacity (Yes or No)	Multi-terrain capacity (Yes or No)			Ref.
						flat	mountainous	underwater	
Carbon nanotube yarn/nylon 6/ polyethylene terephthalate	/	1.54	Yes	Yes	Yes	Yes	Yes	Yes	This work
Silver nano-particle ink/ Paper or PET	2019	10	No	Yes	No	Yes	No	No	2
Liquid crystal networks	2019	0.985	No	No	Yes	Yes	No	No	3
Graphene/ polydimethylsiloxane	2020	0.0024	No	No	Yes	Yes	Yes	Yes	4
Shape memory alloy	2018	3.2	No	No	Yes	Yes	Yes	No	5
Silver nanowire/ polydimethylsiloxane	2017	0.52	No	No	No	Yes	Yes	No	6
Polyvinyl chloride polymer/shape memory alloy wires	2016	140	No	No	No	Yes	No	Yes	7
Polyethylene terephthalate/ink/acrylic	2019	14.29	No	No	No	Yes	No	No	8
Polyvinyl chloride/silver nanowire/polyethylene	2019	0.19	No	No	No	Yes	No	No	9
Liquid-crystal elastomer	2018	0.03	No	No	No	Yes	No	No	10

4. Supplementary movie

Movie S1. Self-crawling soft robot on flat, mountainous, and underwater ground.

The SFSCR contained a 200-μm-thick PET film with an anisotropic bow-shaped structure, with one end having a curvature of 63.3 m^{-1} (forefoot) and the other end being flat (rearfoot). The distance between the two ends was 4.5 cm and the height of the bow was 2.2 cm. A thin composite film of the GSP (mass ratio of graphene/SWNT of 2: 1) coated on the bow-shaped PET film was used as the strain sensor, which was further coated with a thin SEBS film (~37 μm) for sealing. A 3.7 cm long NCY muscle was connected to both ends of the bow-shaped PET film for actuation. To transport heavier loads, the same length of the SCN muscle was also used for actuation.

The SFSCR was demonstrated to crawl in different terrains. (1-3) The SFSCR (NCY muscle) crawled on flat (1), mountainous (2), and underwater surfaces (3) with the aid of zigzag surface pattern by applying 2 W, 2 W, and 6 W electric power, respectively. (4) The SFSCR (SCN muscle) carried 5543 mg load and crawled on a flat surface with the aid of zigzag surface pattern by applying 2 W electric power. (5) The SFSCR (NCY muscle) crawled on underwater surface without the aid of zigzag surface pattern by applying 6 W electric power.

References

1. C. S. Haines, M. D. Lima, N. Li, G. M. Spinks, J. Foroughi, J. D. Madden, S. H. Kim, S. Fang, M. J. De Andrade and F. Göktepe, *Science*, 2014, **343**, 868-872.
2. T. D. Ta, T. Umedachi and Y. Kawahara, 2019.
3. Y. Y. Xiao, Z. C. Jiang, X. Tong and Y. Zhao, *Adv. Mater.*, 2019, **31**, 1903452.
4. X. Wang, B. Yang, D. Tan, Q. Li, B. Song, Z.-S. Wu, A. del Campo, M. Kappl, Z. Wang and S. N. Gorb, *Mater. Today*, 2020, **35**, 42-49.
5. X. Huang, K. Kumar, M. K. Jawed, A. M. Nasab, Z. Ye, W. Shan and C. Majidi, *Sci. Rob.*, 2018, **3**, eaau7557.
6. S. Mao, E. Dong, H. Jin, M. Xu, S. Zhang, J. Yang and K. H. Low, *J. Bionic Eng.*, 2014, **11**, 400-411.
7. H. Jin, E. Dong, M. Xu, C. Liu, G. Alici and Y. Jie, *Smart Mater. Struct.*, 2016, **25**, 085026.
8. J. Li, R. Zhang, L. Mou, M. Jung de Andrade, X. Hu, K. Yu, J. Sun, T. Jia, Y. Dou and H. Chen, *Adv. Funct. Mater.*, 2019, **29**, 1808995.
9. H. Lee, H. Kim, I. Ha, J. Jung, P. Won, H. Cho, J. Yeo, S. Hong, S. Han and J. Kwon, *Soft robot.*, 2019, **6**, 760-767.
10. C. Wang, K. Sim, J. Chen, H. Kim, Z. Rao, Y. Li, W. Chen, J. Song, R. Verduzco and C. Yu, *Adv. Mater.*, 2018, **30**, 1706695.